Stable inversion of gravity anomalies of sedimentary basins with nonsmooth basement reliefs and arbitrary density contrast variations

Valéria C. F. Barbosa*, João B. C. Silva‡, and Walter E. Medeiros**

ABSTRACT

We present a new, stable method for interpreting the basement relief of a sedimentary basin which delineates sharp discontinuities in the basement relief and incorporates any law known a priori for the spatial variation of the density contrast. The subsurface region containing the basin is discretized into a grid of juxtaposed elementary prisms whose density contrasts are the parameters to be estimated. Any vertical line must intersect the basement relief only once, and the mass deficiency must be concentrated near the earth's surface, subject to the observed gravity anomaly being fitted within the experimental errors. In addition, upper and lower bounds on the density contrast of each prism are introduced a priori (one of the bounds being zero), and the method assigns to each elementary prism a density contrast which is close to either bound. The basement relief is therefore delineated by the contact between the prisms with null and nonnull estimated density contrasts, the latter occupying the upper part of the discretized region. The method is stabilized by introducing constraints favoring solutions having the attributes (shared by most sedimentary basins) of being an isolated compact source with lateral borders dipping either vertically or toward the basin center and having horizontal dimensions much greater than its largest vertical dimension. Arbitrary laws of spatial variations of the density contrast, if known a priori, may be incorporated into the problem

by assigning suitable values to the nonnull bound of each prism.

The proposed method differs from previous stable methods by using no smoothness constraint on the interface to be estimated. As a result, it may be applied not only to intracratonic sag basins where the basement relief is essentially smooth but also to rift basins whose basements present discontinuities caused by faults. The method's utility in mapping such basements was demonstrated in tests using synthetic data produced by simulated rift basins. The method mapped with good precision a sequence of step faults which are close to each other and present small vertical slips, a feature particularly difficult to detect from gravity data only. The method was also able to map isolated discontinuities with large vertical throw.

The method was applied to the gravity data from Recôncavo basin, Brazil. The results showed close agreement with known geological structures of the basin. It also demonstrated the method's ability to map a sequence of alternating terraces and structural lows that could not be detected just by inspecting the gravity anomaly.

To demonstrate the method's flexibility in incorporating any a priori knowledge about the density contrast variation, it was applied to the Bouguer anomaly over the San Jacinto Graben, California. Two different exponential laws for the decrease of density contrast with depth were used, leading to estimated maximum depths between 2.2 and 2.4 km.

INTRODUCTION

A main objective in interpreting gravity data from a sedimentary basin is to map the interface separating the sediments from the basement. Unfortunately, the inversion of the basement relief using gravity data only, although presenting a unique solution for the case of homogeneous sediments (Roy, 1962), is an

ill-posed problem because the solution is unstable. As a result, methods using no stabilizing strategy (e.g., Guspí, 1990; Rao et al., 1994) are of limited practical application.

Under the hypothesis that the sedimentary pack is homogeneous, a common stabilizing strategy is to introduce a certain degree of smoothness in the estimated basement relief. The way of introducing the smoothness constraint is accomplished by (1) producing a relief that is mainly a scaled version of the gravity anomaly (Bott, 1960), (2) applying a low-pass filter to the data (Oldenburg, 1974), (3) using a damping parameter (Pilkington and Crossley, 1986; Leão et al., 1996), or (4) minimizing the modulus of the first derivative of the interface representing the basement relief (Barbosa et al., 1997).

In recent years, substantial effort has been directed toward generalizing some of the above-mentioned methods to incorporate a density contrast varying with depth. Most of the methods implementing this generalization are extensions of Bott's (1960) or Oldenburg's (1974) methods and pay great attention to the mathematical problem of approximating a known discrete variation of density with depth by a continuous function yet pay little attention in ascertaining solution stability. Extensions of Bott's (1960) method replace the gravity response of a set of homogeneous prisms (modeling the sedimentary pack) by the response of a set of prisms with density contrast decreasing linearly (Agarwal, 1971; Murthy and Rao, 1979), exponentially (Granser, 1987; Chai and Hinze, 1988), quadratically (Rao, 1986), parabolically (Rao et al., 1993), or hyperbolically (Rao et al., 1994). If the sediment compaction is severe, the density contrast at the bases of the prisms may become very small or even disappear so that the prisms' thicknesses may increase infinitely without changing the fitted anomaly. In this case, generalizations of Bott's method will be unstable. Extensions of Oldenburg's (1974) method allow the density contrast to decrease linearly (Reamer and Ferguson, 1989), exponentially (Granser, 1987), or according to a polynomial law (Guspí, 1992). As in the original Oldenburg (1974) method, the stability of these extensions is achieved by applying a low-pass filter to the data, introducing, in this way, a certain degree of smoothness on the estimated basement relief.

Regardless of assuming homogeneous or depth-dependent density contrasts, methods incorporating smoothness on the estimated relief may be adequately applied only to interpret data from sedimentary basins actually exhibiting this attribute, for example, intracratonic sag basins. To broaden the possibility of successful estimation of nonsmooth basement reliefs, Barbosa et al. (1999) present a stable method to interpret gravity data from basins associated with extensional tectonics where flat bases and steep borders are expected to occur. However, in rift basins, where sequences of small step faults, or alternate sequences of terraces and structural lows very close to each other are common, Barbosa et al.'s (1999) method does not improve the relief resolution as compared with methods incorporating the smoothness constraint.

We present a new, stable method for mapping basement reliefs exhibiting small step faults. The basement is assumed to be homogeneous, whereas the sediments may be heterogeneous. The subsurface region containing the relief is discretized into elementary prismatic cells whose density contrasts are the parameters to be estimated. The solution is stabilized by imposing that any vertical line intersect the relief just once and the mass deficiency be as close as possible to the surface, subject to

the gravity anomaly being fitted within the experimental error. Lower and upper bounds for the density contrast of each cell are also required to stabilize the solutions, one of the bounds being zero. The estimated density contrast of each cell is forced to be close to either bound. The cells containing estimated nonnull density contrasts tend to occupy the shallowest part of the discretized region, and the relief is delineated by the contact between the cells with null and nonnull estimated density contrasts. Because the density contrast estimate for each cell is forced to be close to either bound, this relief is, in general, sharply defined. By properly defining the density contrast bounds for the cells, a priori information about any variation of this contrast with depth may be introduced. We stress that this stabilization strategy was not defined just to meet some mathematical conditions. Rather, it has a geological meaning: It favors solutions having the attributes (shared by most sedimentary basins) of being an isolated compact source with sharp boundaries dipping either vertically or toward the center of the anomalous mass and having horizontal dimensions much greater than its largest vertical dimension.

The method's ability to detect fine structures such as sequences of step faults having small slips is demonstrated with synthetic data. The method was also applied to the gravity anomaly from Recôncavo basin, Brazil. The results show close agreement with known structures and demonstrate the method's ability to detect alternating sequencies of terraces and local structural lows at the basin borders. To illustrate the method's flexibility in incorporating any a priori law for the spatial variation of the density contrast, it is applied to the gravity anomaly over the San Jacinto Graben, California, using the density contrast variation laws given by Cordell (1973) and Chai and Hinze (1988), producing a relief with maximum estimated depths of 2.2 and 2.4 km, respectively.

METHODOLOGY

Inverse problem formulation

Let $\mathbf{g}^o$ be a set of N gravity observations over a sedimentary basin with heterogeneous sediments and homogeneous basement. To estimate the density contrast distribution within this basin, a finite region R enclosing it is divided into M juxtaposed, 2-D, rectangular elementary prisms (Figure 1). The dimensions of the jth prism, b_j and h_j, along the x- and z-directions, respectively, are known and the density contrast of each prism is constant. The x-axis is positioned at the mean topographic surface.

The problem of estimating a constrained parameter vector $\mathbf{p}$ containing the prisms' density contrasts using just $\mathbf{g}^o$ can be formulated as the minimization of the functional

$$\phi^g[\mathbf{g(p)}, \mathbf{g}^o] = \frac{1}{N}\|[\mathbf{g}^o - \mathbf{g(p)}]\|^2, \qquad (1)$$

where $\| \cdot \|$ is the Euclidean norm and $\mathbf{g(p)}$ is an N-dimensional vector containing the fitting gravity anomaly defined by

$$\mathbf{g(p)} = \mathbf{Ap}, \qquad (2)$$

where $\mathbf{A} \equiv \{a_{ij}\}$ is the $N \times M$ matrix of Green's functions whose element a_{ij} is the contribution of the jth prism to the ith observation with unit density contrast. In the case of a very irregular topography, equation (2) is modified to take into account the irregularities on the top of the elementary sources at the uppermost row of elementary cells of the interpretation model.

Finding a vector of parameters $\mathbf{p}^*$ that minimizes functional (1) is an ill-posed problem, characterized by unstable solutions. To transform this ill-posed problem into a well-posed one, we introduce the following assumptions: (1) any vertical line intersects the basement relief only once, (2) the anomalous source is concentrated about the mean topographic surface, and (3) the anomalous source may be represented by a distribution of density contrasts of elementary prisms, where the density contrast of each prism is constrained to assume a value close to a lower or an upper bound, both specified a priori for each prism. These assumptions translate the meaningful geological constraint that the basin is an isolated and compact source with sharp vertical or inward-dipping boundaries and having horizontal dimensions much greater than its largest vertical dimension.

This constrained problem is solved by the following iterative method. Start with an initial approximation $\mathbf{p}_{(0)}$ to the density contrast vector very close to the null vector. Then we look for a constrained parameter perturbation $\Delta\mathbf{p}_{(0)}$ that must affect mainly the parameters close to the surface and partially explain the gravity anomaly. This perturbation is added to $\mathbf{p}_{(0)}$, leading to the approximation $\mathbf{p}_{(1)}$. The anomaly produced by the current approximation is removed from the observations $\mathbf{g}^o$, yielding a residual anomaly which is now used in computing a new perturbation that must partially explain the residual anomaly and affect mostly the parameters close to the surface. At each iteration, each element of the parameter vector $\mathbf{p}$ is forced to assume a value close to a lower or an upper bound (specified a priori for each elementary prism). In this way, the final solution will present most of the deficiency of mass concentrated in a compact way about the mean topographic surface and will depart from the null solution by the amount just necessary to explain the observed anomaly. In addition, the final solution will present lateral borders dipping either vertically or toward the anomalous center of mass. This occurs because the residual anomaly decreases with each iteration and, at all iterations, the method tends to place the anomalous density contrasts as close as possible to the surface so that the number of elementary prisms located at a given horizontal row and having nonnull density contrasts will be smaller than the number for the row immediately above it.

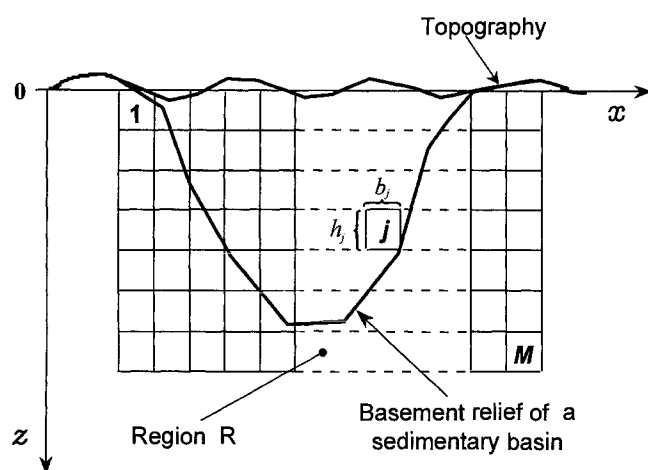The mathematical details of the method are described in the Appendix A.

FIG. 1. Subsurface region R containing the sedimentary basin discretized into M elementary 2-D prisms with width b_j and thickness h_j.

SYNTHETIC DATA APPLICATION

The method produces good results in interpreting not only basement reliefs, which are mostly smooth with a few local discontinuities, but also basements, which are discontinuous overall.

Overall smooth basement with local discontinuities

Figure 2a shows 215 equispaced noise-corrupted Bouguer anomaly observations (dots) in the interval $x \in$ [100 km, 314 km] produced by a simulated 2-D sedimentary basin with a uniform density contrast of -0.3 g/cm^3 relative to a complex basement whose relief is shown in Figure 2b (thick line). The pseudorandom noise is Gaussian, with zero mean and a standard deviation of 0.5 mGal. This model is based on an interpretive geologic cross-section of the Recôncavo basin, Brazil, reported by Milani (1985).

We subdivide the gravity profile into seven data windows (see Appendix A for details about processing by windows). The limits of the data windows are shown in Table 1. Each data window is associated with a source window consisting of the subsurface region defined in the same x-interval of the corresponding data window and in the z-interval [0 km, 6 km]. These source windows are discretized into juxtaposed, 2-D, rectangular elementary prisms with dimensions equal to 1 km and 0.5 km along the x- and z-directions, respectively. For all source windows, we set the upper boundary, $\mathbf{p}_{max}$, to null vector $\mathbf{0}$ and assigned to the elements of $\mathbf{p}_{min}$, the lower boundary, the value -0.3 g/cm^3.

The final interpreted profile is shown in Figure 2b, where the density contrast of each prism is represented as a percentage of the assumed density contrast (which in this case coincides with the true one). The basement relief is considered to be the contact between the cells with null and nonnull estimated density contrasts. The results show an estimated relief very close to the true simulated relief (thick line in Figure 2b)—not only where the true basement topography is smooth but also at the steep discontinuities simulating normal faults. Figure 2a shows the fitted gravity anomaly.

Overall discontinuous basement

Figure 3a shows, in the interval $x \in$ [0 km, 40 km], 41 noise-corrupted gravity observations (dots) sampled in a regular interval of 1 km. The noise is Gaussian, has zero mean, and has a standard deviation of 0.5 mGal. This anomaly is produced by a simulated 2-D sedimentary basin with a density contrast of -0.2 g/cm^3 relative to a basement whose relief is shown in Figure 3b. The actual relief shows a remarkable asymmetric structural low, controlled by normal faults, which in the deepest

Table 1. Synthetic example. Interval along x of the seven data windows used to process the gravity profile in Figure 2 and the corresponding Lagrange multipliers $\lambda(\delta)$.

Data window	Interval along x (km)	$\lambda(\delta)$
1	100–137	30.0
2	120–175	10.0
3	155–185	1.0
4	160–220	10.0
5	200–250	4.0
6	210–270	30.0
7	250–314	20.0

portion of this basin ($z > 4$ km) present a dip angle of 48° and a slip of 2.25 km. In the interval $z \in [0$ km, 4 km] two different faulting patterns are present. Between $x \in [36$ km, 37 km] the basement is controlled by a synthetic fault with dip angle of 70° and slip of 4 km, defining a rather steep basin border. On the other hand, in the interval $x \in [0$ km, 20 km] there is a complex sequence of synthetic and antithetic faults with small slips (<1 km), producing a much smoother relief (average declivity of 11°) when compared with the other border.

In applying the algorithm, we used a single data window in the interval $x \in [0$ km, 40 km] with the source window limited laterally by this same interval and vertically by the interval $z \in [0$ km, 7 km]. This region was discretized into elementary rectangular juxtaposed prisms with dimensions of 0.5 km along both x- and z-directions. We set $\mathbf{p}_{max} = 0$ g/cm^3 and assigned to the elements of $\mathbf{p}_{min}$ the value -0.2 g/cm^3. The result is shown in Figure 3b, where the estimated density contrast of each prism is represented as a percentage of the assumed density contrast (in this case, coinciding with the true one). The fitted anomaly is shown in Figure 3a (solid line). Figure 3b shows the excellent performance of the method in estimating both the steep and the smooth borders. Particularly at the smooth border, the method

produced a good definition of several small discontinuities—a feature rather difficult to detect using inversion methods stabilized by smoothness constraints.

FIELD EXAMPLES

Recôncavo Basin

Figure 4 shows the Bouguer anomaly map of Recôncavo basin in northeast Brazil, corrected for deep crustal effects, Leão et al. (1996) assume this anomaly is produced by the basement relief.

The Recôncavo basin is one of the grabens belonging to the aborted intracontinental Recôncavo–Tucano–Jatobá rift system opened during Early Cretaceous south Atlantic rifting. The basin framework is strongly controlled by several northeast- and northwest-trending normal faults which segmented the basement relief into a complex mosaic of blocks. It is part of a Brazilian regional extensional basin system whose origin is related to the breakup of Gondwana. The gravity fault system presents high dip angles (Milani and Davison, 1988).
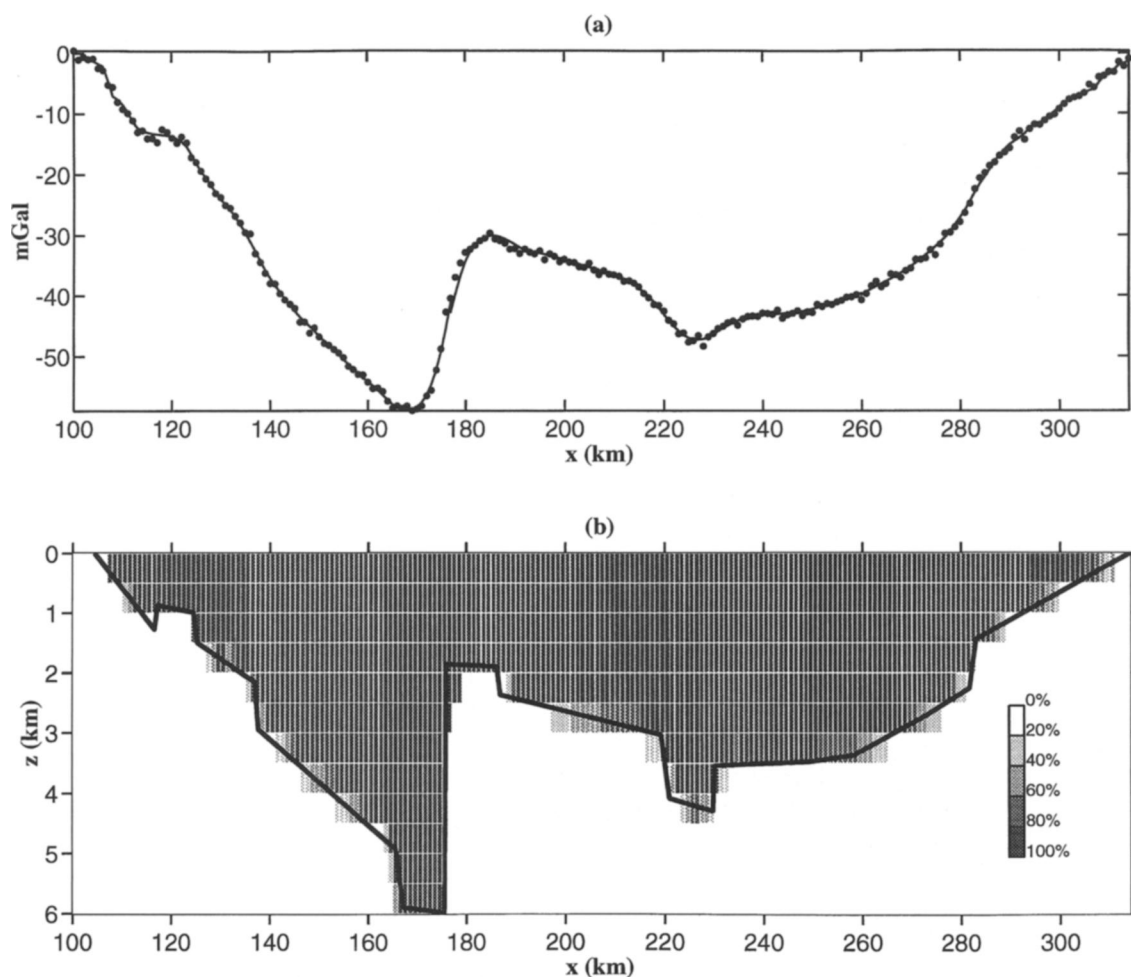

FIG. 2. Simulated overall smooth basement with local discontinuities. (a) Noise-corrupted Bouguer anomaly (dots) and fitted anomaly (solid line). (b) True basement relief (solid thick line) and inversion result in percentage of the assumed density constrast (-0.3 g/cm^3).

Figure 5a shows the Bouguer anomaly (dots) along profile AA' (see location in Figure 4), which was digitized directly from the gridded data of Figure 4 at regular intervals of 1 km, producing a total of 50 data points. The gravity profile was subdivided into four data windows, each associated with a source window limited horizontally by the same intervals defining the data windows and vertically by the interval $z \in$ [0 km, 8 km]. The source windows were discretized into rectangular, 2-D, juxtaposed elementary prisms with dimensions equal to 0.5 km along both the x- and z-directions. The limits of each data window are shown in Table 2. We assumed a constant density contrast of -0.26 g/cm³ between the sediments and the basement. So we set $\mathbf{p}_{max} = \mathbf{0}$ g/cm³ and assigned to the elements of $\mathbf{p}_{min}$ the value -0.26 g/cm³ for all source windows.

Table 2. Recôncavo basin. Interval along x of the four data windows used to process the gravity profile in Figure 4 and the corresponding Lagrange multipliers $\lambda(\delta)$.

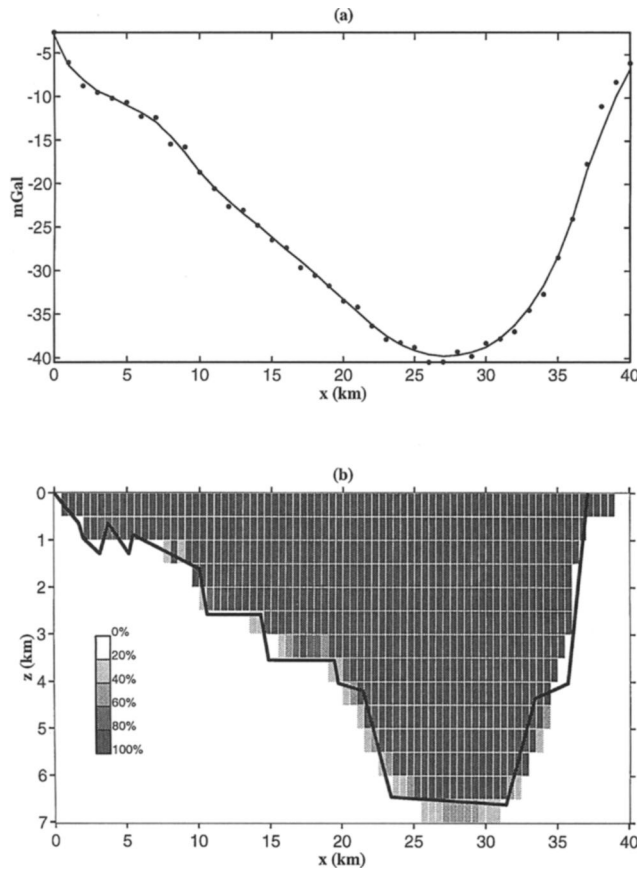| Data window	Interval along x (km)	$\lambda(\delta)$
1	0–20	0.2
2	5–30	0.3
3	20–35	0.1
4	25–49	0.8

FIG. 3. Simulated overall discontinuous basement. (a) Noise-corrupted Bouguer anomaly (dots) and fitted anomaly (solid line). (b) True basement relief (solid thick line) and inversion result as a percentage of the assumed density contrast (-0.2 g/cm³).

The results are shown in Figure 5b, where the estimated density contrast of each prism is represented as a percentage of the assumed density contrast. The fitted gravity anomaly as a solid line is shown in Figure 5a. We note the presence of three important features. The first one is a structural low in the northwestern portion [coinciding with the known Alagoinhas structural low (AL)], showing steep borders and a slightly flat bottom whose maximum depth attains 7 km. In addition, there is an asymmetry between the gradients of the two fault-controlled borders. The gradients in the northwest and southeast borders are, respectively, 42° and 23°. The second geological feature is a low, in the southeastern portion around the coordinate $x = 40$ km, which coincides with the known Miranga structural low (MI). The third feature consists of two terraces inferred by the presence of low gradient areas separating a small and narrow low at $x = 27$ km. The first terrace (Q) occurs in the interval [18 km, 25 km], coinciding with a known feature named Quiricó Platform. The second terrace (MA) is located between $x = 32$ km and $x = 36$ km and is correlated with the Mata-Araçás Terrace. On the other hand, the structural low (U) close to $x = 27$ km is not correlated with any known geological feature.

For comparison, we show in Figures 6b and 7b the inversion results of the gravity anomaly profile AA' using Barbosa et al.'s (1997, 1999) methods, respectively, adapted for inversion of 2-D sources (dashed lines). Barbosa et al.'s (1997) method favors solutions displaying an overall smoothness on the estimated relief, whereas Barbosa et al.'s (1999) method favors solutions exhibiting reliefs with flat bottoms and very steep borders. In Figures 5a, 6a, and 7a, all anomaly fittings are equally acceptable, so the corresponding estimated reliefs may
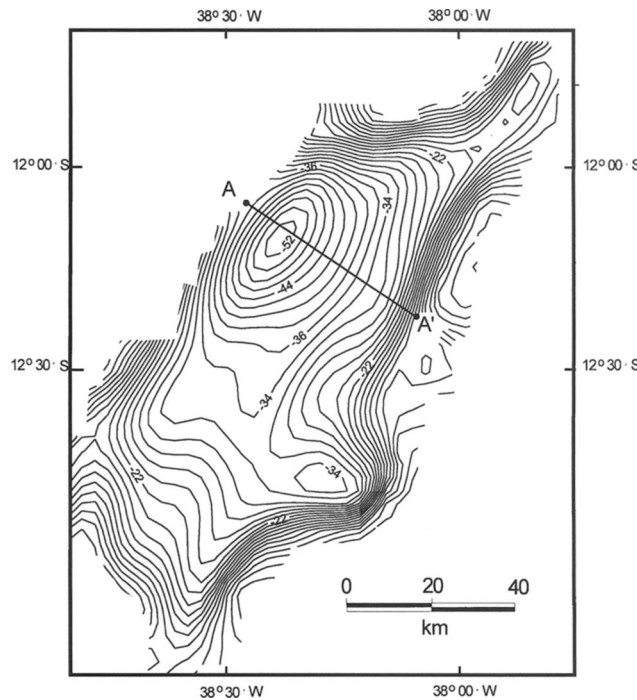

FIG. 4. Recôncavo basin. Bouguer anomaly produced by the basement relief according to Leão et al. (1996). Line segment AA' establishes the location of the gravity profile shown in Figures 5, 6, and 7. Contour interval: 2 mGal.

be considered alternative solutions. In this way, the interpreter must distinguish among them on the basis of the available geological information. That is, no method may be considered superior or inferior; rather, each method should be regarded as adequate or inadequate for interpreting the data from the specific geologic environment. Observe that in delineating the Alagoinhas structural low (between coordinates $x = 5$ km and $x = 20$ km), the degree of smoothness in the relief is high in Figure 6b, intermediate in Figure 5b, and low in Figure 7b. Because the Recôncavo basin is an aborted rift where high-angle faults are expected to occur, the smooth solution shown in Figure 6b is, from the geological viewpoint, the least compatible among the solution triad. On the other hand, the remaining solutions (Figures 5b and 7b) are both compatible with the geologic environment because dip angle faults up to 70° have been reported for the area (Santos and Braga, 1989).

Because the Recôncavo basin is asymmetric with the smallest average gradient on the southeastern portion, small step faults and alternating sequences of terraces and structural lows close to each other are expected to occur in this portion. So the structural features on the southeastern portion (Q, U, and MA in Figure 5b) are geologically meaningful and not just mathematical artifacts. Note that the other two methods do

not clearly delineate these structures because the latter show up in Figures 6b and 7b just as subtle gradient changes in the estimated relief.

Thus, in basin sectors where small step faults and alternating sequences of terraces and structural lows are expected to occur, our method presents superior performance compared with Barbosa et al.'s (1997, 1999) methods. The detection of feature U illustrates that the use of the geologically adequate method may improve the geophysical interpretation.

San Jacinto Graben

Figure 8a shows the Bouguer anomaly (dots) over the San Jacinto Graben, Riverside County, California. This application is intended to exemplify the method's ability in incorporating a priori information about the variation of sediment density with depth.

We removed from the gravity anomaly presented by Cordell (1973) a constant base level of -1.4 mGal to make the anomaly approach zero at the borders and used just one data window in the interval $x \in [0.32$ km, 10 km]. The source window, limited by this interval and by the interval $z \in [0$ km, 3 km], was discretized into elementary prisms with dimensions of 0.25 and 0.125 km along the x- and z-directions, respectively. We performed two tests using, respectively, the following a priori information about the density contrast variation with depth in
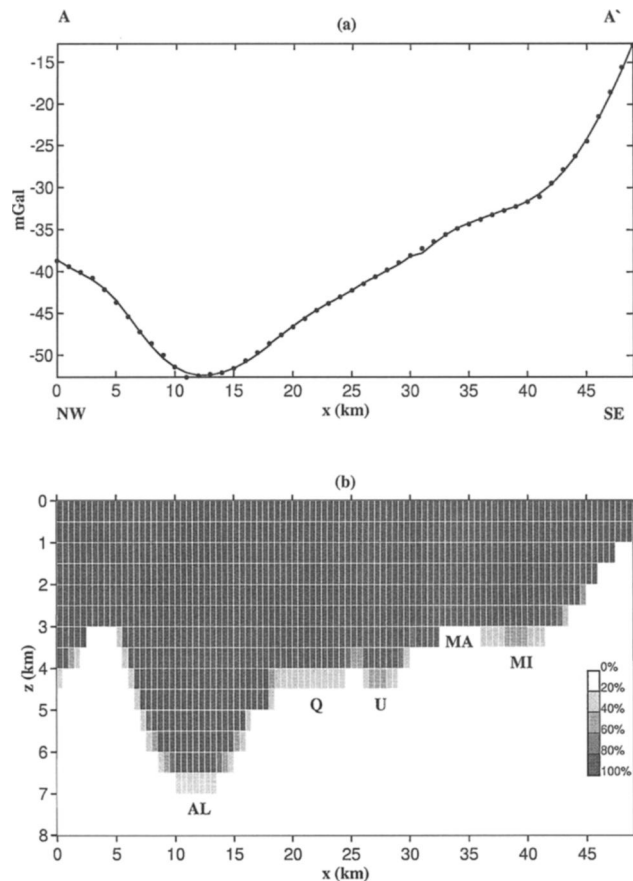

FIG. 5. Recôncavo basin. (a) Observed (dots) and fitted (solid line) Bouguer anomalies along profile AA′ whose location is shown in Figure 4. (b) Inversion result in percentage of the assumed homogeneous density contrast (-0.26 g/cm³). AL—Alagoinhas structural low; Q—Quiricó Platform; MA—Mata-Araçás Terrace; MI—Miranga structural low; U—structural low not correlated with any known geological feature.
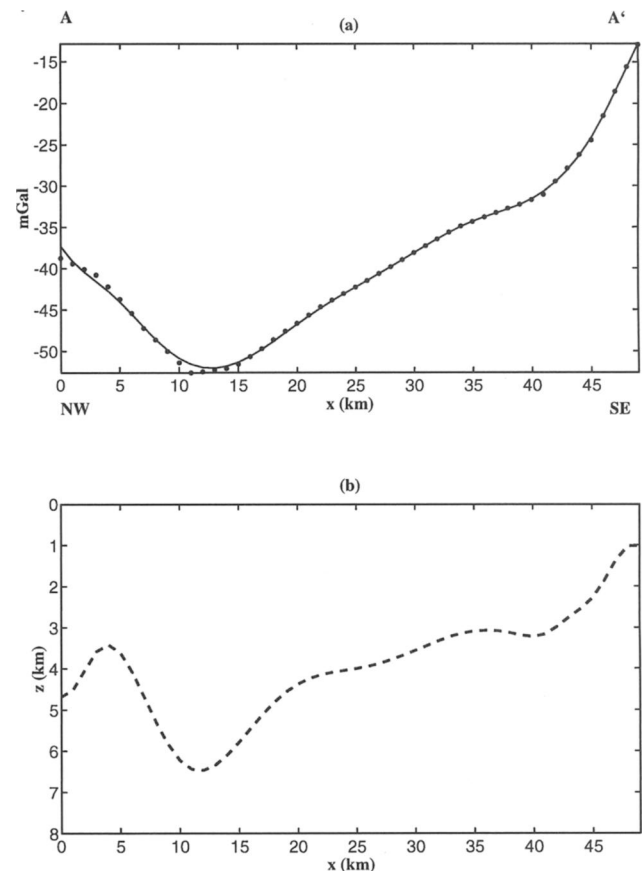

FIG. 6. Recôncavo basin. (a) Observed (dots) and fitted (solid line) Bouguer anomalies along profile AA′ whose location is shown in Figure 4. (b) Result of inversion using Barbosa et al.'s (1997) method (dashed line), which imposes an overall smoothness on the estimated relief.

the San Jacinto Graben:

$$p_{\min_j} = -0.08 - 0.42e^{-0.522\,z_j}, \qquad (3)$$

reported by Chai and Hinze (1988), and

$$p_{\min_j} = -0.55e^{-0.5\,z_j}, \qquad (4)$$

reported by Cordell (1973), where z_j is the z-coordinate of the jth elementary prism center and $p_{\min_j}$ is the lower bound of the jth elementary prism density contrast. In both tests we set $\mathbf{p}_{\max} = 0$ g/cm^3.

The results incorporating the laws of density contrast variation with depth given in equations (3) and (4) are shown in Figures 8b and 9b, and the corresponding fitted gravity anomalies are shown in Figures 8a and 9a, respectively. The percentages shown in Figures 8b and 9b are relative to the value $p_{\min_j}$ established via equations (3) and (4), respectively, to each elementary prism. In accordance with the results reported by Medeiros and Silva (1996), we found in both tests a strikingly asymmetric basement topography. The southwestern border is steeper than the northeastern border because of the large vertical displacement of the faulted blocks between $z = 0.25$ km and $z = 1.75$ km and close to $x = 4$ km. In contrast, on the northeastern border a smaller vertical diplacement is evidenced between $z = 0.375$ km and $z = 1.0$ km and close to $x = 8$ km. Between $x = 6$ km and $x = 8$ km the basement relief is smooth. Similar

to the results of Medeiros and Silva (1996), we found neither a negative nor a positive basement warping around $x = 6.5$ km, as reported by Cordell (1973) and Chai and Hinze (1988), respectively. The main difference between the two tests lies on the graben bottom topography. In Figure 8b, the estimated bottom is narrow and curved, similar to Chai and Hinze's (1988) interpretation; in Figure 9b, a slightly wider and flatter bottom is displayed, analogous to the results reported both by Cordell (1973) and Medeiros and Silva (1996).

CONCLUSIONS

We have presented a stable method for mapping an interface separating two media, assuming the lower medium is homogeneous and the upper medium may be heterogeneous. The subsurface region containing the interface is discretized into elementary cells, and the method estimates the interface as the contact separating the cells with null and nonnull estimated density contrasts. The foundation of solution stabilization is the assumption that the mass deficiency is compact and concentrated about an axis coinciding with the mean topographic surface.

The method requires no assumption about the smoothness of the basement relief. So it is expected to produce geologically meaningful results in interpreting anomalies over (1) intracratonic sag basins where tensile stress is not enough to overcome
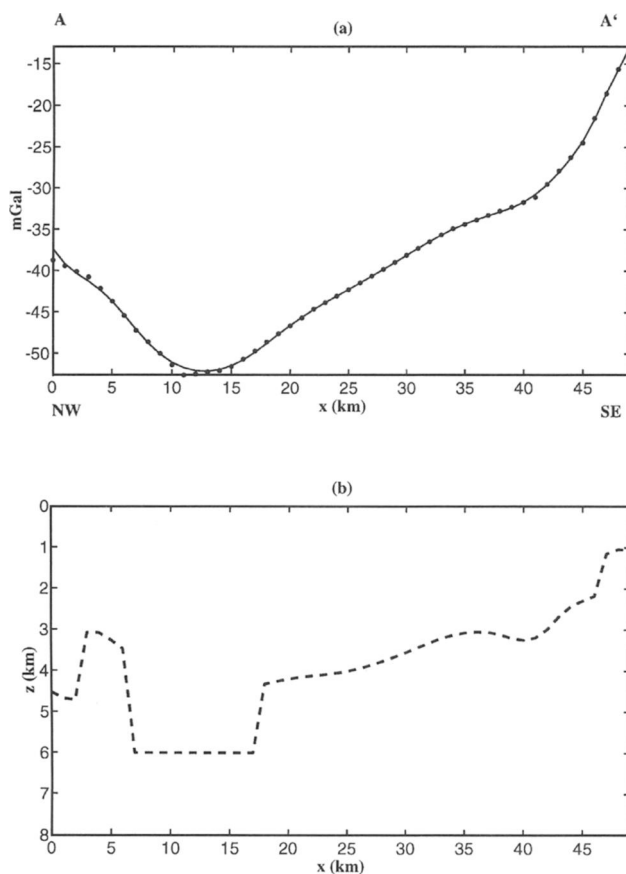

FIG. 7. Recôncavo basin. (a) Observed (dots) and fitted (solid line) Bouguer anomalies along profile AA' whose location is shown in Figure 4. (b) Result of inversion using Barbosa et al.'s (1998) method (dashed line), which favors solutions displaying flat bases and steep borders.
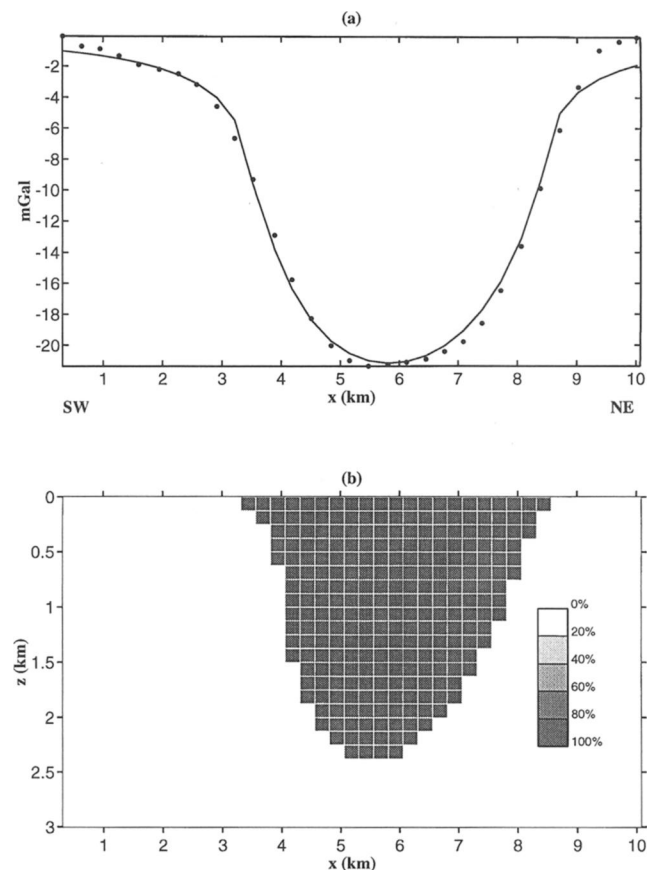

FIG. 8. San Jacinto Graben. (a) Observed Bouguer anomaly according to Cordell (1973) (dots) and fitted anomaly (solid line). (b) Inversion result assuming the exponential law for density contrast variation with depth reported by Chai and Hinze (1988). The percentages are relative to the lower bound assigned to each elementary prism according to equation (3).
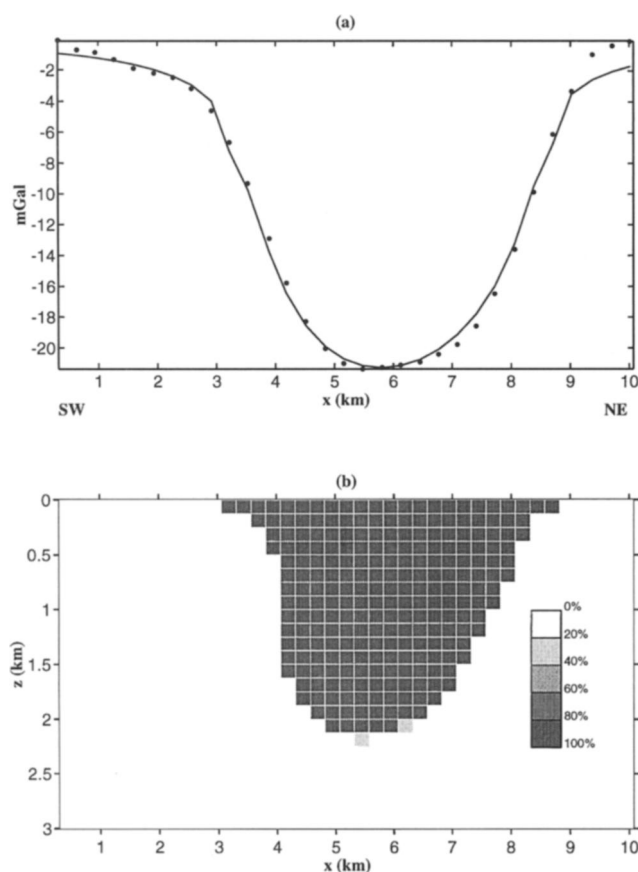
FIG. 9. San Jacinto Graben. (a) Observed Bouguer anomaly according to Cordell (1973) (dots) and fitted anomaly (solid line). (b) Inversion result assuming the exponential law for density contrast variation with depth reported by Cordell (1973). The percentages are relative to the lower bound assigned to each elementary prism according to equation (4).

density contrast variation is known. We stress that a continuous law for the density contrast variation (such as exponential or hyperbolic) is not needed; only the knowledge of the density contrast at discrete points such as those obtained at boreholes is necessary. The continuous law may be used just as an interpolator to obtain the density contrasts at the depth of each cell.

We stress that in the proposed method, the variation of the density contrast with depth is taken into account without modifying the theoretical expression of the gravity anomaly produced by the elementary cell defining the interpretation model. This variation is incorporated by combining the inequality constraints with the freezing process. As a result, the method remains stable even when the law describing the density contrast imposes a null density contrast below a given depth. Evidently, in this case the estimated relief is not the contact between Precambrian and Phanerozoic rocks but is a more recent interface. The method will be unstable in the case of a deep basin with very small density contrasts assigned to several lowermost rows of cells because their contribution to the observed anomaly will be negligible.

Because the a priori information used to stabilize the solutions is very general, the method may also be applied to map a wide variety of geological discontinuities associated with an upper medium exhibiting the stabilizing attribute, that is, being a compact source with vertical or inward-dipping boundaries and having horizontal dimensions greater than the largest vertical dimension. Examples include the crust-mantle interface and a weathering layer. The anomalous source in these examples is usually wider than the data profile. In this case, region R should be extended beyond the gravity profile to avoid edge effects.

Presently, the a priori geological constraints that may be mathematically incorporated into the geophysical inverse problem are too restrictive to hold at all points of a given geological environment. A sedimentary basin, for example, may evolve through several and complex stages so that a method associated with a particular constraint (e.g., smoothness) may produce meaningful geological results on a limited portion of the basin where the imposed constraint is compatible with the actual geologic setting. Usually, a specific method is applied to a whole basin and the results are, likewise, accepted for the whole basin. However, we suggest that the interpreter apply several methods incorporating different constraints to the whole basin and accept the particular inversion results only in subareas where the compatibility between the constraints and the actual geology is presumed to hold. The partial results accepted for the subareas can then be combined to produce a final interpretation.

rock strengh and produce fracture, leading to an overall smooth basement relief, and (2) rift basins where crustal stretching leads to the development of a system of faults and, as a result, to a discontinuous basement relief. In the first case, the results are equivalent to those obtained with Barbosa et al.'s (1997) method; however, the latter is operationally simpler, particularly for 3-D sources. In the second case, besides mapping large isolated discontinuities as in Barbosa et al.'s (1999) method, the main contribution of the present method over all previous methods is its ability to accurately map small discontinuities in the basement relief which are close together and are not trivially inferred from the gravity anomaly just from inspection. However, where very steep borders and flat bottoms are expected to occur, Barbosa et al.'s (1999) method produces better results.

Our method requires a priori information about the source density contrast. This information is easily incorporated to the problem by assigning to each elementary cell upper and lower bounds to the density contrast and requiring that the estimates be frozen at either bound. We illustrated the cases of constant density contrast and density contrast decreasing with depth. Information about more complex density contrast distributions may also be incorporated as far as the law describing the

REFERENCES

Agarwal, B. N. P., 1971, Direct gravity interpretation of sedimentary basin using digital computer, I: Pure Appl. Geophys., 86, 5–12.
Barbosa, V. C. F., and Silva, J. B. C., 1994, Generalized compact gravity inversion: Geophysics, 59, 57–68.
Barbosa, V. C. F., Silva, J. B. C., and Medeiros, W. E., 1997, Gravity inversion of basement relief using approximate equality constraints on depths: Geophysics, 62, 1745–1757.

———1999, Gravity inversion of a discontinuous relief stabilized by weighted smoothness constraints on depth: Geophysics, **64**, scheduled for September/October.

Beck, J. V., and Arnold, K. J., 1977, Parameter estimation in engineering and science: John Wiley & Sons, Inc.

Bott, M. H. P., 1960, The use of rapid digital computing methods for direct gravity interpretation of sedimentary basins: Geophys. J. Roy. Astr. Soc., **3**, 63–67.

Chai, Y., and Hinze, W. J.,1988, Gravity inversion of an interface above which the density contrast varies exponentially with depth: Geophysics, **53**, 837–845.

Cordell, L.,1973, Gravity analysis using an exponentially density-depth function–San Jacinto Graben, California: Geophysics, **38**, 684–690.

Granser, H., 1987, Three-dimensional interpretation of gravity data from sedimentary basins using an exponential density-depth function: Geophys. Prosp., **35**, 1030–1041.

Guillen, A., and Menichetti, V., 1984, Gravity and magnetic inversion with minimization of a specific functional: Geophysics, **49**, 1354–1360.

Guspí, F., 1990, General 2D gravity inversion with density contrast varying with depth: Geoexploration, **26**, 253–265.

———1992, Three-dimensional Fourier gravity inversion with arbitrary density contrast: Geophysics, **57**, 131–135.

Last, B. J., and Kubik, K.,1983, Compact gravity inversion: Geophysics, **48**, 713–721.

Leão, J. W. D., Menezes, P. T. L., Beltrão, J. F., and Silva, J. B. C., 1996, Gravity inversion of basement relief constrained by the knowledge of depth at isolated points: Geophysics, **61**, 1702–1714.

Medeiros, W. E., and Silva, J. B. C., 1996, Geophysical inversion using approximate equality constraints: Geophysics, **61**, 1678–1688.

Milani, E. J., 1985, Characteristics of the tectonic evolution of the Recôncavo and south Tucano basins, Bahia, Brazil: Masters thesis, Federal Univ. Ouro Preto, Brazil (in Portuguese).

Milani, E. J., and Davison I., 1988, Basement control and transfer tectonics in the Recôncavo–Tucano–Jatobá rift, northeast Brazil: Tectonophysics, **154**, 41–70.

Murthy, I. V. R., and Rao, D. B., 1979, Gravity anomalies of two-dimensional bodies of irregular cross-section with density contrast varying with depth: Geophysics, **44**, 1525–1530.

Oldenburg, D. W., 1974, The inversion and interpretation of gravity anomalies: Geophysics, **39**, 526–536.

Pilkington, M., and Crossley, D. J., 1986, Determination of crustal interface topography from potential fields: Geophysics, **51**, 1277–1284.

Rao, C. V., Chakravarthi, V., and Raju, M. L., 1993, Parabolic density function in sedimentary basin modeling: Pure Appl. Geophys., **140**, 493–501.

Rao, C. V., Pramanik, A. G., Kumar, G. V. R. K., and Raju, M. L., 1994, Gravity interpretation of sedimentary basins with hyperbolic density contrast: Geophys. Prosp., **42**, 825–839.

Rao, D. B., 1986, Modeling of sedimentary basins from gravity anomalies with variable density contrast: Geophys. J. Internat., **84**, 207–212.

Reamer, S. K., and Ferguson, J. F., 1989, Regularized two-dimensional Fourier gravity inversion method with application to the Silent Canyon caldera, Nevada: Geophysics, **54**, 486–496.

Roy, A., 1962, Ambiguity in geophysical interpretation: Geophysics, **27**, 90–99.

Santos, C. F., and Braga, J. A. E., 1989, The state of the art of Recôncavo basin, *in* Seminars on Exploratory Interpretation 1: Petrobras, **1**, 45–55 (in Portuguese).

APPENDIX A

MATHEMATICAL DETAILS OF THE METHOD

At the kth iteration, the method looks for a constrained parameter perturbation given by

$$\Delta \mathbf{p}_{(k)} = \mathbf{T}_{(k)} \Delta \mathbf{p}^\dagger_{(k)}, \qquad (A-1)$$

where the unconstrained parameter perturbation $\Delta \mathbf{p}^\dagger_{(k)}$ minimizes the functional

$$\phi(\Delta \mathbf{p}^\dagger) = \frac{1}{N} \left\| \mathbf{W}^{1/2}_{e(k)} [\mathbf{g}^o - \mathbf{A}\mathbf{p}_{(k)} - \mathbf{A}\mathbf{T}_{(k)}\Delta \mathbf{p}^\dagger_{(k)}] \right\|^2$$
$$+ \lambda(\delta) \frac{1}{M} \left\| \mathbf{W}^{1/2}_{P(k)} \mathbf{T}_{(k)} \Delta \mathbf{p}^\dagger_{(k)} \right\|^2. \qquad (A-2)$$

The transformation matrix $\mathbf{T}_{(k)}$ and vector $\Delta \mathbf{p}^\dagger_{(k)}$ are related to a change of variables designed to incorporate into the solution the inequality constraints

$$\mathbf{p}_{min} < \mathbf{p} < \mathbf{p}_{max}, \qquad (A-3)$$

element by element. This procedure is described in detail in Appendix B. The terms $\mathbf{W}_{P(k)}$, $\mathbf{W}_{e(k)}$, λ, and δ are described below.

The matrix $\mathbf{W}_p$ is a diagonal positive-definite weighting matrix defined in parameter space that incorporates the assumption that the anomalous deficiency of mass is concentrated about the earth's surface. This geological constraint may be mathematically incorporated into the inverse problem by minimizing the moment of inertia of the sources about the x-axis. This procedure is a particular case of the scheme introduced by Guillen and Menichetti (1984). So the jth diagonal element of matrix $\mathbf{W}_{P(k)}$ is

$$w_{p_{j(k)}} = \frac{v_j \left(\frac{h_j^2}{12} + z_j^2 \right)}{|p_{j(k)}| + \epsilon}, \qquad j = 1, 2, \ldots, M, \quad (A-4)$$

where v_j is the area of the jth prism, z_j is the z-coordinate of the center of the jth prism, $p_{j(k)}$ is the jth element of vector $\mathbf{p}_{(k)}$, and ϵ is a small positive number of the order of 10^{-7}.

The value $\mathbf{W}_{e(k)}$ is a diagonal positive-definite weighting matrix in observation space whose ith element is given by (Last and Kubik, 1983)

$$\mathbf{W}^{-1}_{e(k)_{ii}} = \sigma^2 \, \mathrm{diag}\left\{ \mathbf{A}[\mathbf{W}_{P(k)}]^{-1} \mathbf{A}^T \right\}, \qquad i = 1, 2, \ldots, N, \quad (A-5)$$

where σ is an estimate of the standard deviation of noise in data and the superscript T stands for transposition. The parameter $\lambda(\delta)$ is a Lagrange multiplier (nonnegative scalar), and δ is the expected mean square of the noise realizations in data. The value of $\lambda(\delta)$ is selected to produce a data misfit compatible with the presence of noise in data.

We obtain an approximation for the estimate $\Delta \hat{\mathbf{p}}^\dagger_{(k)}$ in two steps [from now on, we use the hat symbol ($\hat{\ }$) to denote estimates]. The first step consists of differentiating $\phi(\Delta \mathbf{p}^\dagger)$ in equation (A-2) with respect to $\Delta \mathbf{p}^\dagger_{(k)}$ (neglecting the dependence of $\mathbf{W}_{P(k)}$ and $\mathbf{W}_{e(k)}$ on $\mathbf{p}$) and setting the result equal to the null vector, obtaining

$$\Delta \hat{\mathbf{p}}^\dagger_{(k)} = \mathbf{T}^{-1}_{(k)} \mathbf{H}_{(k)} \mathbf{j}_{(k)}, \qquad (A-6)$$

where $\mathbf{T}$ in the transformation matrix to incorporate the inequality constraints; the inverse operator matrix is

$$\mathbf{H}_{(k)} = \mathbf{W}^{-1}_{P(k)} \mathbf{A}^T \left(\mathbf{A}\mathbf{W}^{-1}_{P(k)} \mathbf{A}^T + \lambda(\delta)\mathbf{W}^{-1}_{e(k)} \right)^{-1}; \quad (A-7)$$

and the data misfit vector

$$\mathbf{j}_{(k)} = \mathbf{g}^o - \mathbf{A}\hat{\mathbf{p}}_{(k)}. \qquad (A-8)$$

In deriving equation (A-7), we use the matrix identity (Beck and Arnold, 1977)

$$(\mathbf{C}^T\mathbf{D}^{-1}\mathbf{C} + \mathbf{B})^{-1}\mathbf{C}^T\mathbf{D}^{-1} = \mathbf{B}^{-1}\mathbf{C}^T(\mathbf{C}\mathbf{B}^{-1}\mathbf{C}^T + \mathbf{D})^{-1},$$

(A-9)

where $\mathbf{C}$ is a generic matrix and $\mathbf{B}$ and $\mathbf{D}$ are generic but nonsingular matrices.

The second step consists of forcing the anomalous source to be compact. To this end, $\hat{p}_{j_{(k+1)}}$ is tentatively frozen at the upper or the lower bound by assigning a very large value (on the order of $1/\epsilon$) to the jth diagonal element of $\mathbf{W}_{p_{(k+1)}}$ when $\hat{p}_{j_{(k+1)}}$ is, respectively, greater than $p_{\max_j} - \nu$ or smaller than $p_{\min_j} + \nu$ (where ν is a small positive number on the order of 10^{-2}). A crucial point in the algorithm convergence is the undesirable possibility of premature freezing of some parameter estimates at either bound, particularly at the upper one, $\mathbf{p}_{\max} = \mathbf{0}$ (null vector). Because the starting tentative solution is close to the null vector, some parameter estimates have to creep to the lower bound along the iterations. However, this may not happen because matrix $\mathbf{T}_{(k)}$ may be near singular (see Appendix B) so that these parameters might be assigned large perturbations $\Delta\hat{p}_{j_{(k)}}^\dagger$. Since these perturbations may be either positive or negative, they may push some of the corresponding estimates $\hat{p}_{j_{(k)}}^\dagger$ in the correct direction, that is, toward the lower bound, but other estimates may be contingently pushed in the opposite direction, that is, toward the upper bound. As a result, these estimates may be prematurely frozen at the upper bound and not explain the gravity data. Further improvement in data fitting will only be possible by moving these parameters back to the lower bound, which would be an extremely slow process because any large change in parameter perturbation would be prevented by the value $1/\epsilon$ assigned to elements of $\mathbf{W}_{p_{(k+1)}}$. To avoid any premature freezing and accelerate the iteration convergence, we decrease the modulus of the unconstrained perturbations $\Delta\mathbf{p}_{(k)}^\dagger$ by compelling the modulus to be equal to the modulus of the constrained perturbation $\Delta\mathbf{p}_{(k-1)}$.

The final estimator is given by

$$\Delta\hat{\mathbf{p}}_{(k)}^\dagger = \frac{\mathbf{T}_{(k)}^{-1}\mathbf{H}_{(k)}\mathbf{j}_{(k)}}{\left|\mathbf{T}_{(k)}^{-1}\mathbf{H}_{(k)}\mathbf{j}_{(k)}\right|} \cdot |\Delta\hat{\mathbf{p}}_{(k-1)}|.$$

(A-10)

The value $\Delta\hat{\mathbf{p}}_{(k)}^\dagger$ is estimated by solving equation (A-10) and is added to the approximation $\hat{\mathbf{p}}_{(k)}^\dagger$, producing an estimate for $\mathbf{p}_{(k+1)}^\dagger$. Finally, the estimate $\hat{\mathbf{p}}_{(k+1)}$ is obtained by using the change of variables described in Appendix B (equation B-2).

In contrast with the procedure presented by Barbosa and Silva (1994), the inequality constraints incorporated by this method are rigid, that is, no estimated density contrast is allowed to violate either bound. In interpreting anomalies with gradients smaller than about 1 mGal/km, both methods yield equivalent results. However, for steeper gravity anomaly gradients, Barbosa and Silva's (1994) method fails to produce a compact source because high gravity gradients may be produced by a pair of adjacent cells—one with a very high density contrast and the other one with a very low density contrast, both violating the $\mathbf{p}_{\max}$ and $\mathbf{p}_{\min}$.

Computational procedures

The proposed methodology was implemented in an algorithm consisting of the following steps:

1) Iteration $k = 0$. Set $\mathbf{p}_{\max} = \mathbf{0}$ and make $\mathbf{W}_{p_{(0)}}$ and $\mathbf{W}_{e_{(0)}}$ equal to the identity matrix. Input the elements of $\mathbf{p}_{\min}$ and the initial approximation $\mathbf{p}_{(0)}$ satisfying the inequality constraints. We recommend setting $p_{j_{(0)}} = p_{\min_j}/100$, $j = 1, \ldots, M$.

2) Obtain $\hat{\mathbf{p}}_{(k)}^\dagger = f(\hat{\mathbf{p}}_{(k)})$ by using the change of variables described in Appendix B (equation B-1).

3) Obtain $\Delta\hat{\mathbf{p}}_{(k)}^\dagger$ using equation (A-10).

4) Obtain $\hat{\mathbf{p}}_{(k+1)}^\dagger = \hat{\mathbf{p}}_{(k)}^\dagger + \Delta\hat{\mathbf{p}}_{(k)}^\dagger$.

5) Compute $\hat{\mathbf{p}}_{(k+1)}$ by using the change of variables described in equation (B-2).

6) If $k \leq 6$, go to step 7; otherwise, test for the algorithm convergence. Evaluate

$$s_{(k)} = \frac{1}{6}\sum_{i=1}^{6}\left\|\hat{\mathbf{p}}_{(k+1-i)} - \hat{\mathbf{p}}_{(k-i)}\right\|.$$

(A-11)

If $s_{(k)}$ is equal to or smaller than a given threshold value τ and functional (1) evaluated at the $(k+1)$st iteration is equal to or smaller than the expected noise mean square δ, the iteration is stopped; otherwise, go to step 7.

7) Update the elements of $\mathbf{W}_{p_{(k)}}$ and $\mathbf{W}_{e_{(k)}}$ in one of the following ways: If $\hat{p}_{j_{(k+1)}}$ is smaller than $p_{\max_j} - \nu$ and larger than $p_{\min_j} + \nu$, obtain the jth diagonal elements of matrices $\mathbf{W}_{p_{(k+1)}}$ and $\mathbf{W}_{e_{(k+1)}}$ according to equations (A-4) and (A-5), respectively. Otherwise, assign a very large value (on the order of $1/\epsilon$) to the jth elements of $\mathbf{W}_{p_{(k+1)}}$ and obtain the jth element of $\mathbf{W}_{e_{(k+1)}}$ according to equation (A-5). Increment k and go to step 2.

Practical implementation

The large dimension of the matrix $\mathbf{A}\mathbf{W}_{p_{(k)}}^{-1}\mathbf{A}^T + \lambda(\delta)\mathbf{W}_{e_{(k)}}^{-1}$, dictated by the great number of observations, sometimes makes it impractical to evaluate $\Delta\hat{\mathbf{p}}_{(k)}^\dagger$ using equation (A-10). This difficulty is aggravated by the fact that equation (A-10) must be solved iteratively. To overcome this difficulty, we subdivide a large profile into smaller ones (referred to as data windows) and process them sequentially. Accordingly, the discretized subsurface region containing the anomalous sources is also subdivided into smaller subregions (referred to as source windows). To avoid edge effects, we extend horizontally each source window beyond the data window limits by at least 50% of the corresponding data window extent (except for the case of a single source window). Additionally, we impose an overlap of at least 15% between adjacent data windows. Upon processing all data windows, parts of the overlapping source windows containing the estimated density contrasts and parts of the corresponding overlapping segments of the fitted anomaly are eliminated so that the remaining parts produce a final, continuous interpreted profile exhibiting minimum edge effects between conterminous windows. Note, for example, in Figures 2a and 2b the absence of edge effects at the borders of the data and source windows, respectively.

In all applications presented in this paper, we used the following parameters: $\epsilon = 10^{-7}$, $\nu = 10^{-2}$, and $\tau = 10^{-4}$. In the examples associated with Figures 3, 8, and 9, we used Lagrange multipliers equal to 0.5, 0.1, and 0.1, respectively. In the examples associated with Figures 2 and 5, Tables 1 and 2, respectively, show the x-intervals of the data windows and the corresponding Lagrange multipliers.

APPENDIX B

INCORPORATION OF INEQUALITY CONSTRAINTS

To incorporate the inequality constraints (A-3), we introduce a homeomorphic transformation $f(\mathbf{p})$ that maps the constrained vector $\mathbf{p} \equiv \{p_j\} \in (p_{\min_j}, p_{\max_j})$, $j = 1, 2, \ldots, M$ onto the unconstrained vector $\mathbf{p}^\dagger \equiv \{p_j^\dagger\} \in (-\infty, +\infty)$, $j = 1, 2, \ldots, M$. This transformation is performed element by element, so for the jth parameter we have

$$p_j^\dagger = f(p_j) = -\log\left(\frac{p_{\max_j} - p_j}{p_j - p_{\min_j}}\right). \tag{B-1}$$

The inverse transformation is defined as

$$p_j = f^{-1}(p_j^\dagger) = \frac{p_{\max_j} - p_{\min_j}}{1 + e^{-p_j^\dagger}} + p_{\min_j}. \tag{B-2}$$

Transformation (B-1) is incorporated via equation (A-1), where $\mathbf{T}_{(k)}$ is an $M \times M$ diagonal matrix whose jth element at the kth iteration is

$$T_{jj(k)} = \left(\frac{\partial f(p_j)}{\partial p_j}\bigg|_{p_j = \hat{p}_{j(k)}}\right)^{-1}. \tag{B-3}$$

This replacement is based on the analytic relationship between the total derivatives of the jth elements of $\hat{\mathbf{p}}_{(k)}$ and $\hat{\mathbf{p}}_{(k)}^\dagger$ given by

$$d\hat{p}_{j(k)} = \left(\frac{\partial f(p_j)}{\partial p_j}\bigg|_{p_j = \hat{p}_{j(k)}}\right)^{-1} d\hat{p}_{j(k)}^\dagger. \tag{B-4}$$

Substituting equation (B-1) into equation (B-3), we get

$$T_{jj(k)} = \frac{(\hat{p}_{j(k)} - p_{\min_j})(p_{\max_j} - \hat{p}_{j(k)})}{(p_{\max_j} - p_{\min_j})}. \tag{B-5}$$

Theoretically, $T_{jj(k)}$ in equation (B-5) never assumes a value exactly equal to zero because constraints (A-3) are *strict inequality* constraints. In practice, however, $T_{jj(k)}$ may assume a null value because of round-off errors in evaluating the exponential function in equation (B-2). To prevent null values from occurring in any diagonal element of $\mathbf{T}_{(k)}$, a small positive number ξ (on the order of 10^{-2}) is added to each term of the numerator in equation (B-5).